Structure and Corrosion Behaviour of Al−Nb Alloys

F. Layachi[a], M. Y. Debili[a, *], and H. Bedboudi[a]

[a] *Laboratory of Magnetism and Spectroscopy of Solids LM2S, Department of Physics, Faculty of Science,
Badji Mokhtar Annaba University BP.12, Annaba, 23000 Algeria*
e-mail: mydebili@yahoo.fr

Abstract—Effects of niobium content on the microstructure and corrosion were investigated on various Al−x% Nb alloys (x: 10, 20, 25, 30, 40, and 50 wt %) prepared by high-frequency electromagnetic fusion melting and solidification at room temperature. Microstructural characterization was carried out by X-ray diffraction (XRD), differential scanning calorimetry (DSC), Vickers microhardness, and scanning electron microscopy (SEM). Electrochemical tests in 3.5 wt % NaCl solution, via potentiodynamic polarization curves and impedance spectroscopy (EIS) was accomplished on both as-cast and annealed alloys. All of the results highlight the role played by the intermetallic trialuminide compound Al_3Nb dispersed within the matrix consisting of α-Al solid solution. The volume fraction of the Al_3Nb intermetallic phase controls the mechanical properties through the microhardness acting as reinforcement of the α-Al matrix in the manner of a composite material. It also acts as a precaution against corrosion by the pitting of aluminum. This effect naturally varies according to the niobium content and the distribution of the intermetallic phase.

INTRODUCTION

The addition of an appropriate metal improve properties and leads to a change in the microstructure of aluminum-based alloys which are extensively used in industry fields for reducing energy consumption and pollution [1] and are environmentally friendly because they lead to lower CO_2 emissions [2−5], due to their remarkable properties such as low density (2.71 g/cm^3), high-strength, easy workability, good corrosion resistance in a variety of aggressive environments [6, 7], excellent electrical and thermal conductivities [5]. The melting point of niobium and its good corrosion resistance to NaCl medium [1, 6, 8] are the principal reasons that led us to choose it as an additive element to aluminium. for application in Al-battery systems, anode materials in cathodic protection systems [9], and sacrificial anodes in cathodic protection of steel in seawater [9−13]. Al−Nb alloys which are very attractive for many applications are widely studied by several techniques in literature [6, 8, 14−26] owing to have attracted many considerations as high-temperature structural materials [19, 24] such as turbine components in power plants, spacecraft, stationary gas turbines [15, 19, 25, 27−29] due to their low ductility at room temperature [27], excellent super-conductivity, high elastic stiffness, and strength, also exhibit high oxidation resistance at high temperatures [24, 26, 29, 30]. Several studies have investigated the influence of the addition of suitable TM (transition metal) on electrochemical behavior. Khireche et al. [31] have investigated the addition of Zn and Sn, the aluminum activation depend on the type and proportion of element, by addition of 5 wt % of Zn to pure Al and 5 wt % of Zn with different Sn contents (0.1, 0.2, 0.4 wt %) respectively, this composition may be appropriate for active anodes. Gupta et al. [32] have discussed the effect of Cr addition as allowing addition element on the corrosion behavior in 0.01 M NaCl medium, the addition of Cr leads to improvement of corrosion resistance and hardness with comparison to pure Al and commercial Al, this improvement was attributed to a nanocrystalline structure obtained from the ball milling process and extended solid solubility of Cr in Al, and uniformly distributed fine intermetallic phases in the Al−Cr matrix. Ujah et al. [6] investigated the relationship between corrosion resistance and microstructure, where they did studies on corrosion behavior of Al and Al−x% Nb alloys with x = 1, 4, 8, 12 in acidic and saline media, synthesized by spark plasma sintering and found out Al−1% Nb and Al−4% Nb had good corrosion resistance than pure aluminium in both mediums, the nanocomposite can replace pure Al as a conductor in power transmission conductors, therefore the addition of niobium to aluminium enhances electrical conductivity, strength, and corrosion resistance. Oladijo et al. [33] have discussed the correlation between porosity and corrosion rate of stainless steel, brass, super Invar and Aluminium2xxx alloys, they have demonstrated that the corro-

Table 1. Crystallographic data of phases

Phase	Crystal structure	Lattice parameters, nm	Space group	Protype	Strukturbericht
Al$_3$Nb [42]	Tetragonal	$a = 0.384$ $b = 0.863$	$I4/mmm$	Al$_3$Ti	$D0_{22}$
Al [42]	Cubic	$a = 0.405$	$Fm\overline{3}m$	Cu	A_1
Nb [42]	Cubic	$a = 0.331$	$Fm\overline{3}m$	W	A_2

sion rate decreased with increasing porosity, they have found a low porosity sample make it get better E_{corr}. Kong et al. [34] studied the effect of Nb content on the microstructure and mechanical properties of nickel-based alloys through high-throughput sample fabrication, the grain size of the as-received nickel-based alloys decreased with the Nb content.

In this work, we highlight the effect of the addition of different Nb contents via the intermetallic compound (Al$_3$Nb) formed by congruent fusion from the liquid, as shown in the equilibrium phase diagram [35], on the microstructural evolution as well as electrochemical behavior of Al−x% Nb alloys with (x: 10, 20, 25, 30, 40, and 50 wt %) in 3.5 wt % NaCl solution(seawater equivalent), which exhibits good corrosion resistance compared to other aluminium alloys.

EXPERIMENTAL PART

Al−Nb binary system alloy, in the present work, was fabricated by a high-frequency induction fusion process. In the first time, commercial Al and Nb elemental powder (99.9% purity) were mixed and cold compacted into the cylinder, the density of the product was sufficient to be intended for high-frequency induction fusion (HF). LinnTherm 600 types (300 kHz) and power of 6 kW with a primary vacuum. The samples thus fused and solidified have a mass of 5 g and are cut with a microtome before mechanical polishing with (600−4000) SiC grinding paper and etched with Keller's reagent solution of (5 mL HF + 9 mL HCl + 22 mL HNO$_3$ + 74 mL H$_2$O) for 10 s, then the bulk obtained was treated in the air under the temperature of 500°C at annealing time of 60 min and air-cooled.

The as-elaborated structure was characterized by X-ray diffraction (XRD) using a (Panalytical) diffractometer provided with copper anticathode (λCu = 1.54056 Å). The scanning was made between 20° and 90° with a step size of 0.013°/s. DSC thermo grams were obtained using a DSC type LABSYS EVO with alumina crucibles to heat the sample under argon atmosphere. The samples were heated with a temperature rise rate of 12°C/min in the temperature range 30−800°C. The surface morphologies of the samples before and after the corrosion test were investigated by light microscopy (Nikon ECLIPS LV150N). Scanning electron microscopy SEM FEI Quanta 250 apparatus was used for qualitative and quantitative analysis by energy-dispersive X-ray spectroscopy (EDS). Digital surfMountains®8 software was used to visualize 3D surface morphology. For electrochemical characterization, the surface was mechanically polished with SiC emery paper and subsequently treated to remove the impurities by two successive baths of acetone (99.5%) then ethanol (95%) rinsed in deionized water. Electrochemical measurements were performed using the PARSTAT 4000 instrument, controlled by a microcomputer with Versa Studio software to record the curves of polarization, connected to a cell to three electrodes potentiostat manufactured. The electrochemical cell is amounting to three electrodes. The used electrodes are: the working electrode which is the sample, the reference in saturated calomel electrode (SCE) of KCl ($E = 0.242$ V), and the counter electrode was graphite rode. All the experiment was measured in a corrosive medium by using a solution of sodium chloride (NaCl) at 3.5% for 24 h under potential in open circuit (OCP). The potential that is our equilibrium potential was measured after 24 h. Then polarization curves were recorded with a sweep of an interval −250 at 250 mV, compared with the equilibrium potential, and a 0.5 mV/s scanning speed to record the curve of polarization. The electrochemical measurements were performed at room temperature.

RESULTS AND DISCUSSION

Figures 1a, 1b show the XRD patterns of as-cast and heat-treated Al−Nb alloys which reveal, in addition to the diffraction peaks of the α-Al solid solution, the presence of diffraction peaks related to the intermetallic Al$_3$Nb compound as expected by the equilibrium phase diagram of the Al−Nb system Fig. 2 and Table 1. The solubility of Niobium in aluminium is almost zero [35] and may be subject to discussion in many recent works based on inconsistencies between the most recent assessments [36, 37]. A re-investigation of the solubility limits of the (Nb), AlNb$_3$, AlNb$_2$, and the Nb-rich side of the Al$_3$Nb phases on the Nb−Al system has also been studied [38, 39].
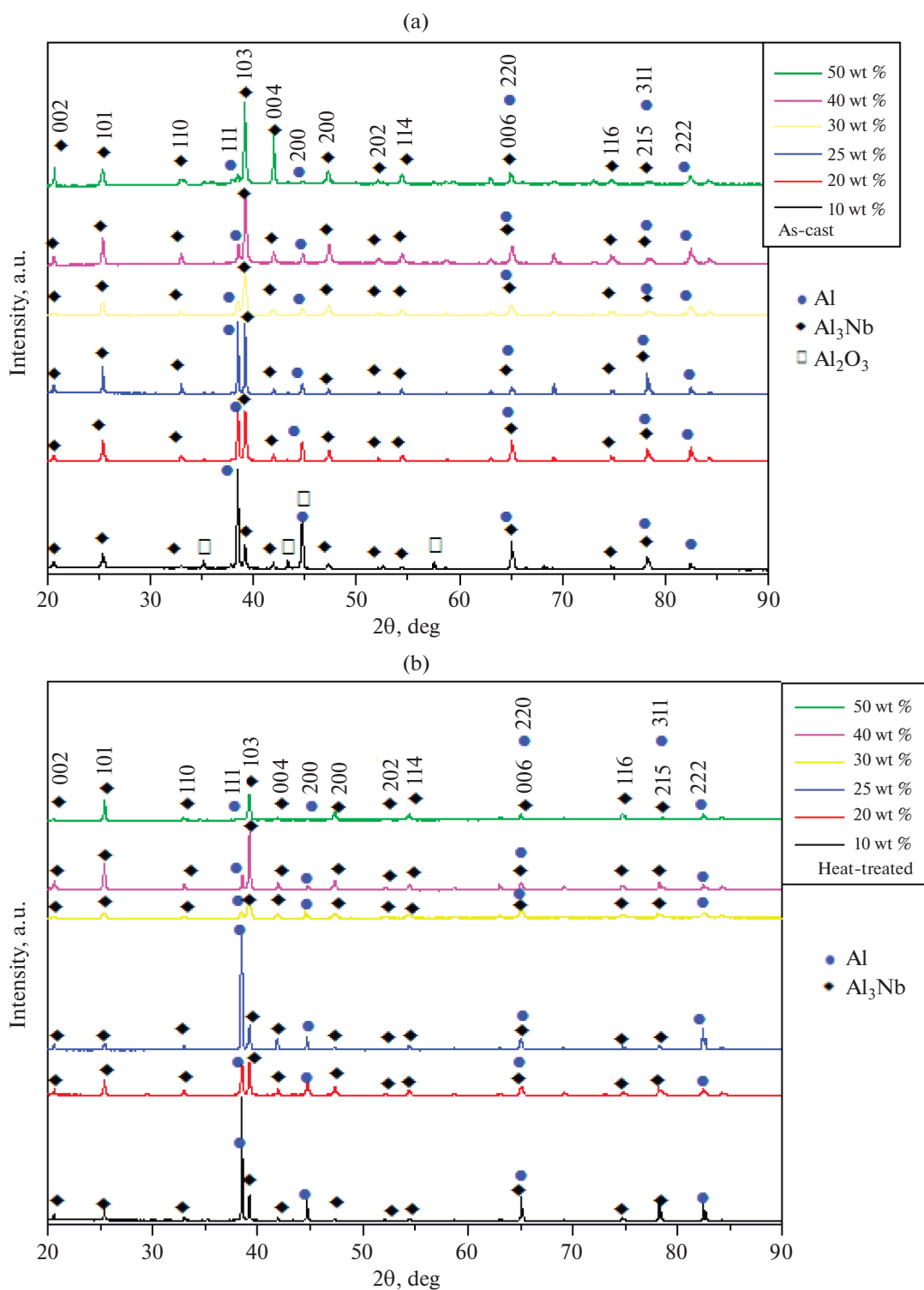
(a)

(b)

Fig. 1. (a) XRD patterns of as-cast samples with different Nb content. (b) XRD patterns of heat-treated samples with different Nb content.

XRD patterns of Al−Nb as-cast and heat-treated alloys indicate the crystallization of the alloys in two phases. Indeed, we note the presence of (111), (200), (220), (311), and (222) peaks corresponding to α-Al according to (JCPDScards 00-004-0787) [40], the intensity of the diffraction peak at 2θ = 38° decreases with the increase of niobium content. Moreover, the intensity of the diffraction peak indexed as (103) of the
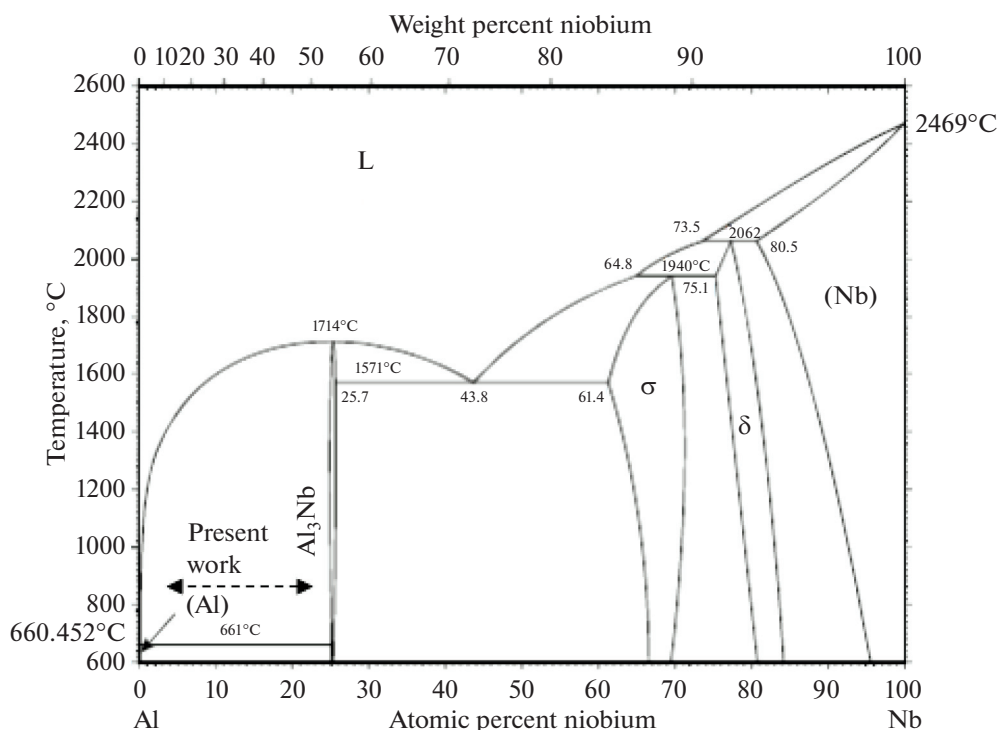
Fig. 2. Equilibrium phase diagram of Al–Nb system [35].

tetragonal phase Al$_3$Nb which appears towards $2\theta = 39°$, increases with niobium content. Diffraction peaks as (002), (101), (110), (103), (004), (200), (202), (114), (006), (116), (215) are related to the tetragonal phase Al$_3$Nb according to (JCPDScards 03-065-4945) [41], similar results have been reported by other authors [16].

X-ray diffraction patterns from Al–Nb as-cast and heat-treated are similar; the decrease in the diffraction peak intensity of aluminum is due to the increase in niobium content. After annealing at 500°C for 1 h, the intensity of Al$_3$Nb phase diffraction peaks increases in turn and could be explained by the increase of trialuminide intermetallic Al$_3$Nb compound volume fraction.

Thermal Analysis

Differential scanning calorimetry (DSC) curves recorded from as-cast Al–Nb alloys from room temperature to 1500°C are similar during heating and show an endothermic melting peak at 660°C corresponding to aluminium Figs. 3a, 3b. Also, there is one exothermic broad peak in the range of 883–1250°C and with a maximum at 1134°C, only in alloy 10 wt % and could be related to the aluminothermic reduction of the pentaoxide of niobium by excess aluminium leading to the formation of Al$_3$Nb intermetallic compound [25] depending on the chemical reaction Al + Nb$_2$O$_5$ → Al$_2$O$_3$ +Al$_3$Nb. Montana et al. [14] observed

an exothermic peak in the range 820–995°C with a maximum at 933°C and they attributed it to Al$_3$Nb according to a reaction with $\Delta G = -40$ kJ/mol. H. Sina et al. [27] studied the formation of aluminides by using a mixture of Al–Nb powder with different compositions of Al, they found another exothermic peak beyond the melting point of aluminum at $800 \pm 20°C$, when a combustion reaction is initiated in fine and coarse Al particles, they concluded that the presence of this peak is attributed to the formation of (Al$_3$Nb) and determined the activation energy for Al$_3$Nb compound formation as 255 ± 26 kJ mol^{-1}, their result was confirmed by SEM. Unlike Al$_3$Ti and Al$_3$V, Al$_3$Nb melts congruently, which facilitates its production in large quantities [39, 43].

However, for all alloys, except 50 and 40 wt %, an anomaly in differential scanning calorimetry has been revealed by the occurrence of a double exothermic peak, only during the cooling step, a position where the aluminium crystallization peak should appear, i.e. around 660°C Fig. 3c, this could be likened to the crystallization of αAl solid solution and αAl–Al$_3$Nb eutectic [44]. This is all the more marked as the niobium content is low i.e. alloy 10 wt %, the effect persists but becomes less pronounced for higher niobium contents i.e. alloy 30 wt % while it disappears for alloy 40 wt % and alloy 50 wt %.

The microhardness of Al–Nb alloys as-cast and heat treated. increases quasilinearly with the content of a harder element (Nb) as shown by Fig. 4, similar
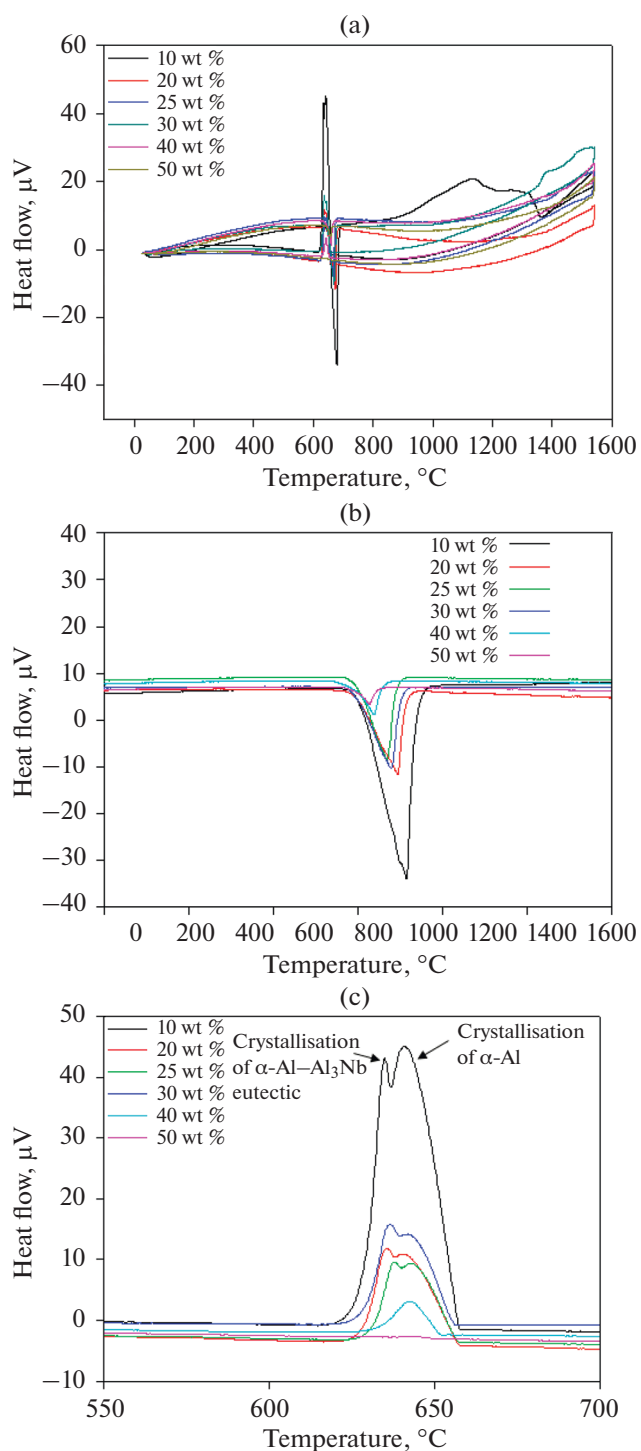
Fig. 4. Microhardness evolution in as-cast and heat-treated specimen versus Niobium content.

Fig. 3. (a) Heating–cooling (whole temperature range). (b) Heating (Partial temperature range) enlarged image. (c) Partial temperature range (cooling) enlarged image.

ness of alloy 30 wt % was ∼10 times higher than that of pure Al (30 HV). The evolution of microhardness of Al–Nb alloys heat-treated is higher than the as-cast; the gap widens further as the niobium content increases which may be attributed to the increase in Al_3Nb volume fraction after heat treatment leading to a composite-like behavior.

The observations of the microstructure by scanning electron microscopy were carried out on the entire as-cast and heat-treated alloys Figs. 5a–5l. Indeed, the structure is made up of two phases essentially α-Al and the intermetallic Al_3Nb dispersed uniformly within the aluminium matrix with a nearly spherical shape and a volume fraction estimated approximately to 70% of the total volume with an average particle size lying between 10 to 30 μm in most alloys except alloy 10 wt % where the secondary Al_3Nb phase has a dendritic morphology well developed in secondary arms [45] and represents almost 30% of the total alloy volume, as well as a eutectic structure visible in the SEM micrograph of Fig. 5a. This particular morphology is also observed in the same alloy after heat treatment at 500°C Fig. 5b. The chemical analysis by EDS done at several particular points of as-cast alloy 10 wt % makes it possible to determine the mass and atomic compositions of Al_3Nb Figs. 6a, 6b and Table 2, αAl matrix Figs. 6c, 6d and Table 3, Al_2O_3 Figs. 6e, 6f and Table 4, global alloy composition Table 5. All niobium was used either to form Al_3Nb phase or to go into solid solution in the aluminum network, but we did not find any pure unmelted or undissolved Niobium particles [46]. Alloy 50 wt % is the niobium richest and its structure is totally different from that of other alloys both in the as-cast and in the heat-treated states. A aluminium solid solution is reduced to a minor phase and therefore confines in the Al_3Nb inter-particle spacing Fig. 7a. The chemical analysis by EDS done at particular points of as-cast

results have been reported by other authors [44–47], this increase can be attributed to the microstructural changes in α-Al matrix by the formation of the primary dendritic structure [16]. The authors [48–51] reported in their studies the relationship between microstructural and mechanical properties. The hard-
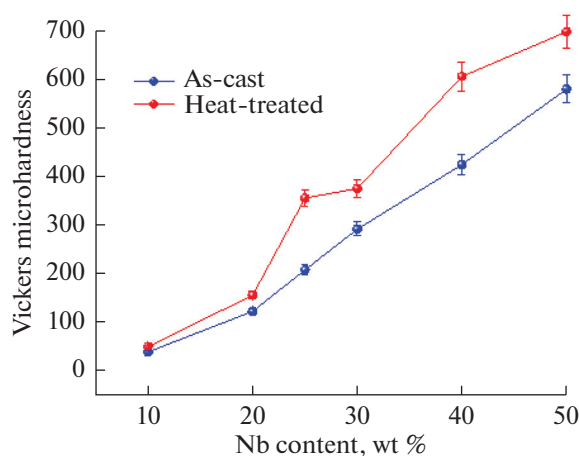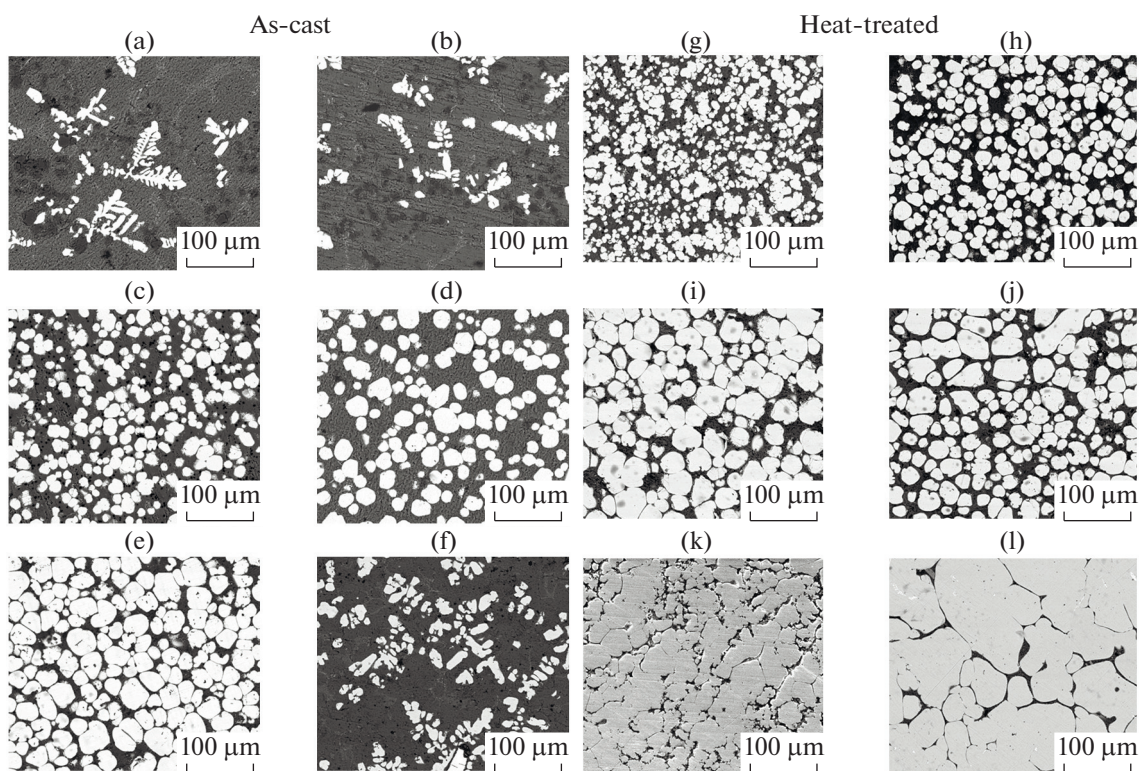
As-cast

Heat-treated

Fig. 5. Microstructure by scanning electron microscopy of as-cast and heat-treated alloys: (a) 10 wt % as-cast; (b) 10 wt % heat-treated; (c) 20 wt % as-cast; (d) 20 wt % heat-treated; (e) 25 wt % as-cast; (f) 25 wt % heat-treated; (g) 30 wt % as-cast; (h) 30 wt % heat-treated; (i) 40 wt % as-cast; (j) 40 wt % heat-treated; (k) 50 wt % as-cast; (l) 50 wt % heat-treated.

alloy 50 wt % permits the determination of the mass and atomic compositions of Al_3Nb which to become the major phase Figs. 7a, 7b and Table 6, α-Al Figs. 6c, 6d and Table 7. Therefore alloy 50 wt % behaves like an intermetallic alloy.

The effects of niobium content on potentiodynamic polarization curves in aluminium matrix of Al−Nb alloys as-cast and heat-treated after immersion for 24 h in 3.5 wt % NaCl solution is presented in a superposition of Tafel plot in Figs. 8a, 8b.

As it can be seen, there is different corrosion behavior of as-cast and heat-treated alloys, the fitted values of β_c, β_a, the corrosion potential (E_{corr}), and the corrosion current density (I_{corr}) of the Al−Nb system were obtained from the polarization curves by extrapolation method of the Tafel curves and listed in Tables 8a, 8b.

Resistance of polarization R_p (kΩ cm²) was determined using the relationship of Stern et Geary [47, 48].

$$R_p = \frac{\Delta E}{\Delta I} = \frac{\beta_a \beta_c}{2.31 I_{corr} (\beta_a + \beta_c)}.$$

Where β_a and β_c are anodic and cathodic tafel slopes respectively, I_{corr} (µA cm⁻²) is a current density.

The corrosion rate CR (mm/yr) was calculated using the Faraday equation [49]

$$CR = K \frac{I_{corr} EW}{d}.$$

Where K is a conversion factor (3.27 × 10⁻³ mm g/(µA cm yr)), I_{corr} the corrosion current density in (µA/cm²), EW the equivalent weight of alloy and d is the density of alloy (g/cm³).

Table 2. EDS quantitative analysis of Al_3Nb (alloy 10 wt % as-cast)

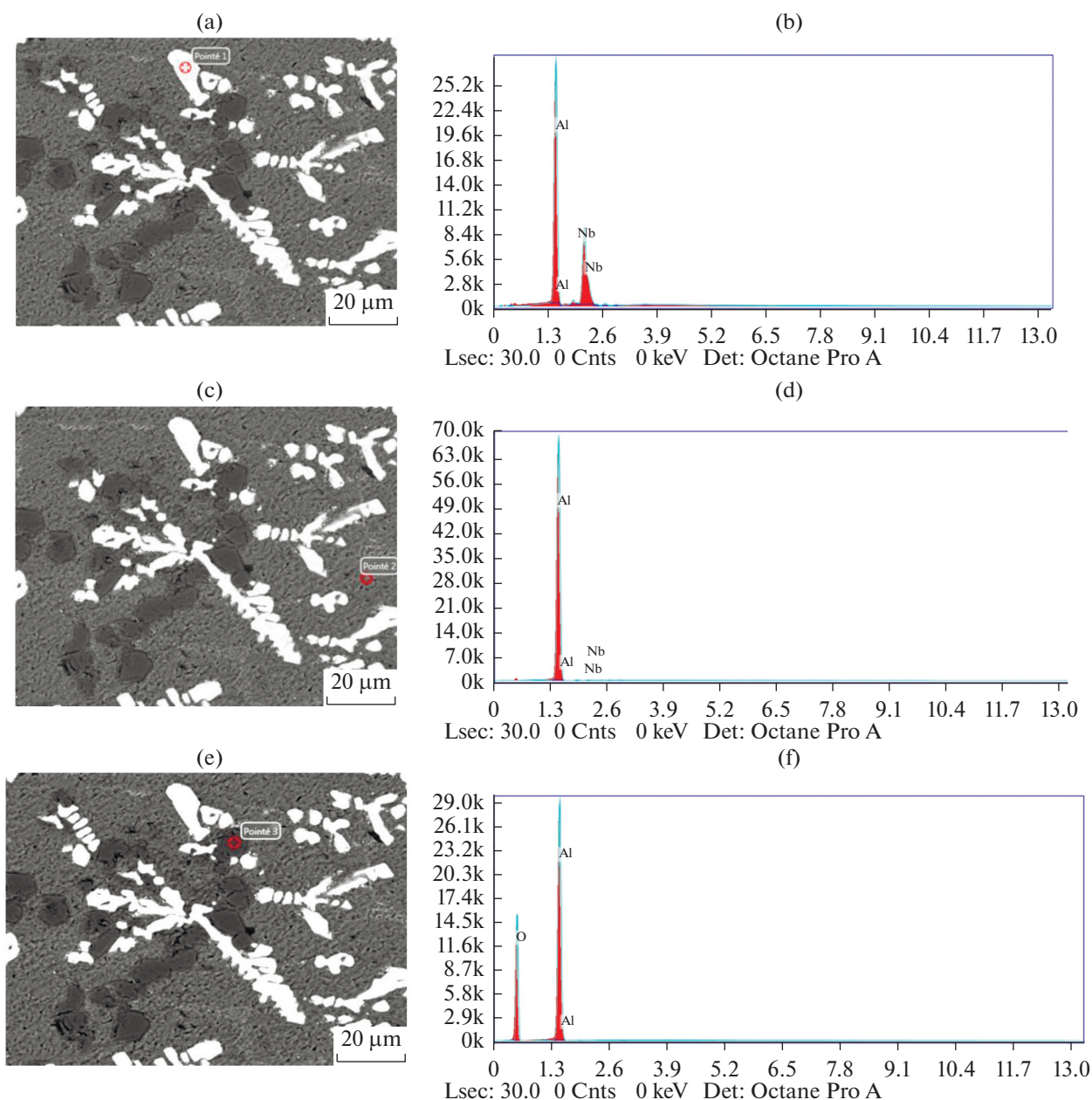| Element	Wt %	At %	Total intensity	Erreur, %	K ratio	Z	A	F
AlK	48.69	**76.57**	6801.10	6.14	0.2791	1.1202	0.5086	1.0060
NbL	51.31	**23.43**	2484.69	5.03	0.2893	0.8890	0.6349	0.9991

(a)

(b)

(c)

(d)

(e)

(f)

Fig. 6. SEM image and EDS analysis of alloy 10 wt % as-cast, (a, b) Al_3Nb, (c, d) α-Al matrix, (e, f) Al_2O_3.

These reactions can occur into the anodic and cathodic electrochemical process, two reactions occur in the anode sites represented by the equation in the reaction below (1) [50]:

$$Al \rightarrow Al^{3+} + 3e, \tag{1}$$

$$Al^{3+} + 3OH^- \rightarrow Al(OH)_3.$$
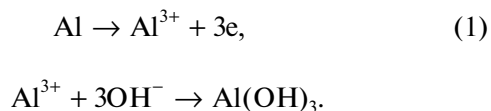
The cathodic reaction in neutral solution of (NaCl) given by the reduction of oxygen is represented in equation (2) [50]: $O_2 + 2H_2O + 4e \rightarrow 4OH^-$.

The results indicated that the pitting potential of alloys increases with the increase of Nb content in the order of 30 wt % as-cast < 40 wt % as-cast < 50 wt % as-cast, so the pitting potential of alloy 50 wt % as-cast is nobler than that of alloy 40 wt % as-cast and alloy 30 wt % as-cast respectively Fig. 9. The removal of the Al atom corresponds to the initiation of pitting [51, 52], from this point of view, the pitting is occurring more quickly than in sample 30 wt % as-cast because it contains the highest proportion of aluminum. The result is confirmed by the value of corrosion rate which increases with the increase of Al content in

Table 3. EDS quantitative analysis of α-Al (alloy 10 wt % as-cast)

Element	Wt %	At %	Total intensity	Erreur, %	K ratio	Z	A	F
AlK	98.42	**99.54**	17260.35	1.35	0.9622	1.0033	0.9743	1.0001
NbL	1.58	**0.46**	34.24	9.91	0.0054	0.7935	0.4329	0.9983

sequence 50 wt % as-cast < 40 wt % as-cast < 30 wt % as-cast Fig. 10. This result is attributed essentially to the difference in the microstructure. Alloy 50 wt % as-cast has high R_p with value equal to 14.63 (kΩ cm²) then that of alloy 30 wt % as-cast and alloy 40 wt % as-cast with values 8.67 (kΩ cm²) and 9.93 (kΩ cm²) respectively, due to the low corrosion current density, consequently therefore the samples 30 wt % as-cast and 40 wt % as-cast have high corrosion rate (CR) values 45.60 × 10⁻³ (mm yr⁻¹) and 38.10 × 10⁻³ (mm yr⁻¹)

respectively then that of sample 50 wt % as-cast with value 29 × 10⁻³ (mm yr⁻¹).

On another hand, the effect of heat treatment for 1 h at 500°C was investigated and shown in Fig. 9, which lead to an increase in the potential towards the noble value with −0.775 V for alloy 30 wt % heat-treated, −0.743 V for alloy 40 wt % heat-treated, and −0.724 V for alloy 50 wt % heat-treated.

The type of aluminum corrosion in seawater is the pitting corrosion [52], it occurs on the surface of the
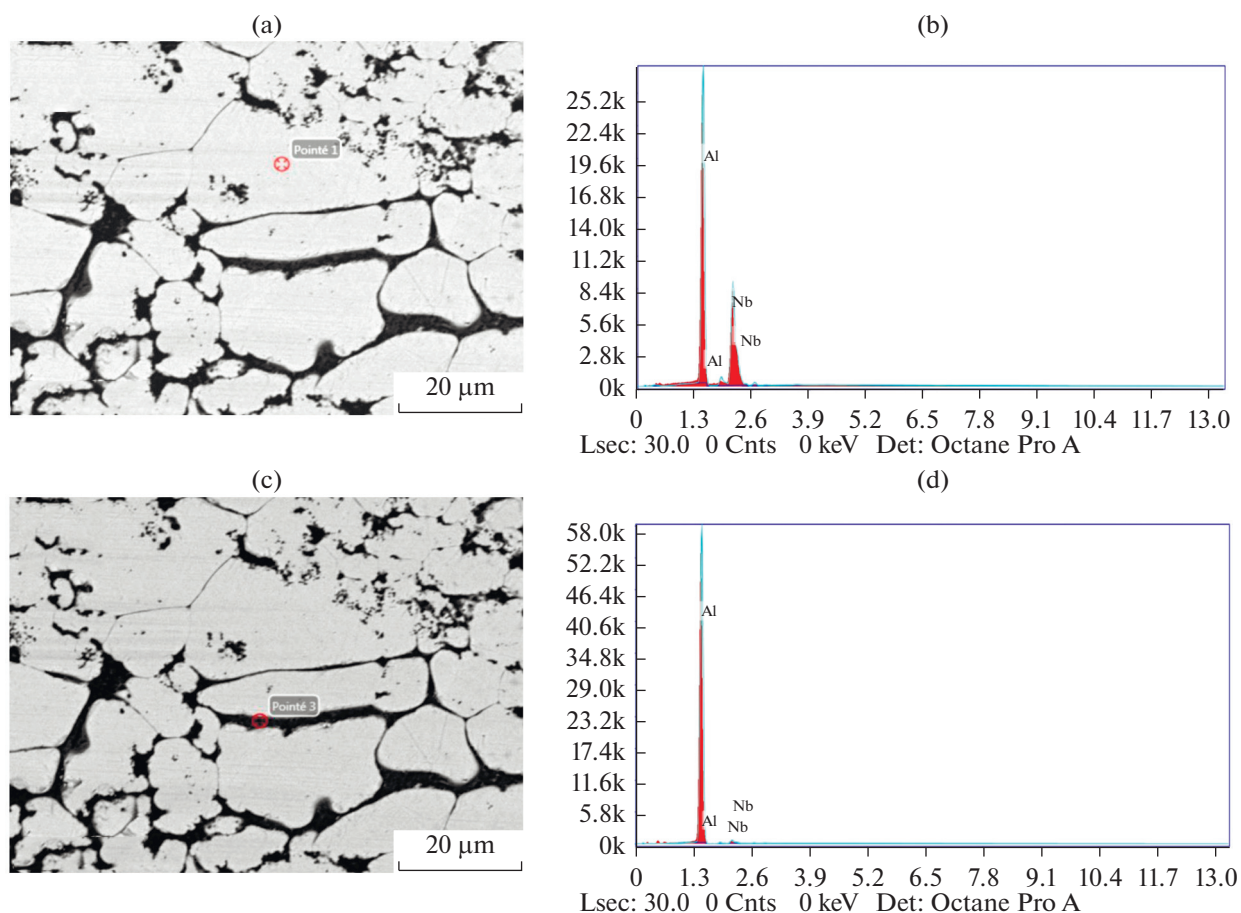

Fig. 7. SEM image and EDS analysis of alloy 50 wt % as-cast, (a, b) Al$_3$Nb, (c, d) α-Al matrix.

Table 4. EDS quantitative analysis of Al_2O_3 (alloy 10 wt % as-cast)

Element	Wt %	At %	Total intensity	Erreur, %	K ratio	Z	A
OK	55.08	**67.41**	2803.45	7.94	0.1923	1.0501	0.3325
AlK	44.92	**32.59**	7250.39	6.05	0.2150	0.9345	0.5120

Table 5. EDS global quantitative analysis (alloy 10 wt % as-cast)

Element	Wt %	At %	Total intensity	Erreur, %	K ratio	Z	A	F
AlK	**89.83**	**96.82**	14904.86	2.58	0.7837	1.0220	0.8529	1.0010
NbL	**10.17**	**3.18**	255.37	7.71	0.0380	0.8088	0.4625	0.9985

metal, the chloride ion Cl^- interact with the region near to work electrode (sample) and causes the decomposition of aluminum matrix [53]. Figures 11a, 11b shows Nyquist plots of Al–Nb alloys as-cast and heat-treated which are evaluated in 3.5 wt % NaCl solution at room temperature. A semi-circle arcs diagram is usually thought of as a mechanism of charge transfer on an inhomogeneous surface [54, 55].

Semi-circle behavior can be understood by assuming an electric equivalent circuit (ECC) for the interface between electronic (electrode) and ionic conducting (electrolyte) materials. EIS data are fitted by EC-Lab® V10.37, and complex equivalent circuit model of samples with different Nb content of as-cast and heat-treated are presented in Fig. 12 and consisted of the resistance (R_s), in series with (Z_{CPE1}) in parallel arrangement with (R_1) and (Z_{CPE2}) which is also in parallel with (R_2), in which R_s is the ohmic resistance of the electrolyte between the working electrode (WE) and reference electrode (RE), in addition, Z_{CPE1} cor-

responds to the capacitance of the oxide layer and R_1 is the polarization resistance of the passive layer. Another factor to consider is the Z_{CPE2} constant phase element due to a double layer capacitance and R_2 is the charge transfer resistance. $Z_{CPE} = 1/(Q(i\omega)^n$, ω is the angular frequency, $\omega = 2\pi f$ and f is the frequency, $n = 0$ corresponds to a pure resistor, $n = 1$ to a pure capacitor and $n = 0.5$ to a Warburg type impedance [56]. Change in n value has been related to porosity and roughness [57]. The diameter of the Nyquist semicircle corresponds to the corrosion resistance. It is important to remark that the highest semicircle arc corresponds to the best electrochemical corrosion behavior. The higher values of R_{ct} indicate the formation of a stable oxide layer on the surface that offers a significant increase in the corrosion resistance of the alloy. Nyquist plots revealed that two dominant processes could be imagined happening in parallel 1 capacitive behavior of charge separation at interface and 2 resistive behavior of electron transfer process. The combination of these two processes results in capacitive

Table 6. EDS quantitative analysis of Al_3Nb (alloy 50 wt % as-cast)

Element	Wt %	At %	Total intensity	Erreur, %	K ratio	Z	A	F
AlK	48.41	**76.37**	6844.43	6.14	0.2770	1.1211	0.5074	1.0060
NbL	51.59	**23.63**	2545.28	4.96	0.2922	0.8897	0.6373	0.9991

Table 7. EDS quantitative analysis of α-Al (alloy 50 wt % as-cast)

Element	Wt %	At %	Total intensity	Erreur, %	K ratio	Z	A	F
AlK	92.77	**97.79**	14483.92	2.20	0.8396	1.0155	0.8906	1.0007
NbL	7.23	**2.21**	159.00	8.00	0.0261	0.8035	0.4507	0.9984

Table 8. Electrochemical parameters

Alloy type	Potential, V_{SCE}	Current density, $\mu A\ cm^{-2}$	Cathodic beta, V_{SCE}	Anodic beta, V_{SCE}	R_p, kΩ cm^2	$C_R \times 10^{-3}$, mm yr^{-1}
(a) of Al−Nb as-cast with different Nb content 3.5% NaCl solution at environmental temperature						
Pure Al	−0.713	0.4	0.216	0.017	18.06	4.36
10 wt %as-cast	−0.867	2.94	0.187	0.270	16.31	31.6
20 wt % as-cast	−0.938	17.23	0.133	0.565	2.719	181.4
25 wt % as-cast	−0.917	4.53	0.172	0.264	10.021	47.1
30 wt % as-cast	−0.897	4.44	0.142	0.234	8.67	45.6
40 wt % as-cast	−0.859	3.82	0.101	0.177	9.93	38.1
50 wt % as-cast	−0.805	3.09	0.198	0.218	14.63	29
(b) of Al−Nb heat-treated with different Nb content 3.5% NaCl solution at environmental temperature						
10 wt % heat treated	−0.887	6.73	0.152	0.333	6.75	72.3
20 wt % heat-treated	−0.849	2.21	0.137	0.188	15.6	23.3
25 wt % heat-treated	−0.837	2.41	0.161	0.128	12.86	25.1
30 wt %heat-treated	−0.775	6.27	0.169	0.051	2.73	64.4
40 wt % heat-treated	−0.743	5.00	0.239	0.044	3.25	49.9
50 wt % heat-treated	−0.724	4.41	0.198	0.065	4.83	42.8

semi-circle response on the Nyquist plot, from which the Nyquist data for 10 and 50 wt % as-cast Fig. 11a, show a good arc-like behavior over the frequency range examined and the diameter of the arc is larger than that of the other samples and is associated with a lower corrosion rate [58, 59], for heat-treated alloys it is 25 and 50 wt %. Different impedance parameters were obtained after fit and are listed in Tables 9a, 9b.

Typical microstructures from optical microscopy micrographs Figs. 13a−13l associated with 3D surface morphology images Figs. 13a'−13l' clearly show that some alloys, in particular 10, 40, and 50 wt % as-cast Figs. 13b−13j−13l and 13b'−13j'−13l', after corrosion test, performs better than before corrosion unlike alloy 20 wt % and alloy 25 wt % as-cast Figs. 13d−13f and 13d'−13f'. This is based on the autonomous actions of
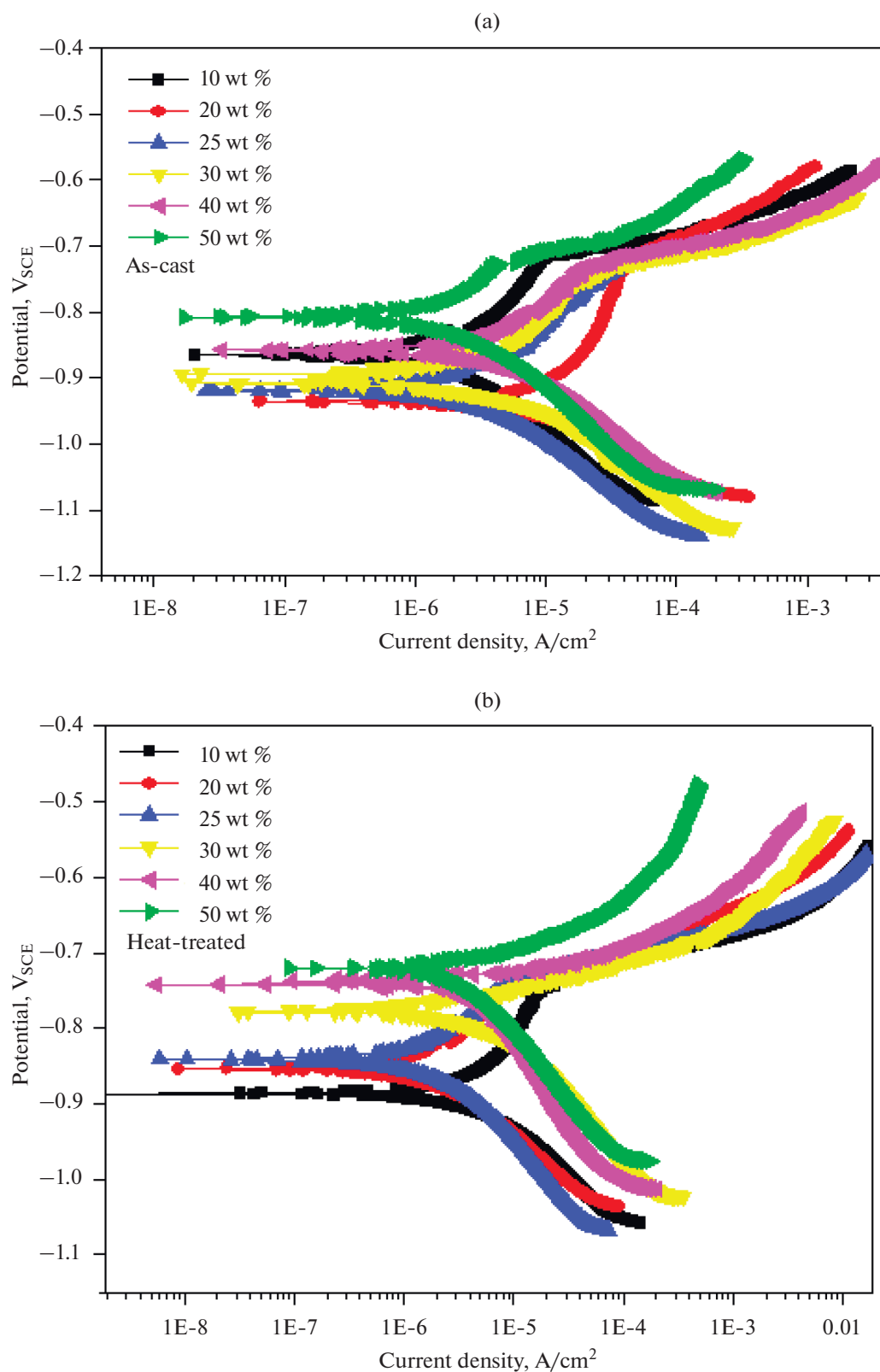
Fig. 8. (a) Potentiodynamic polarization curves of Al−Nb alloy as cast in 3.5 wt % NaCl medium at room temperature. (b) Potentiodynamic polarization curves of Al−Nb heat-treated alloys in 3.5 wt % NaCl medium at room temperature.
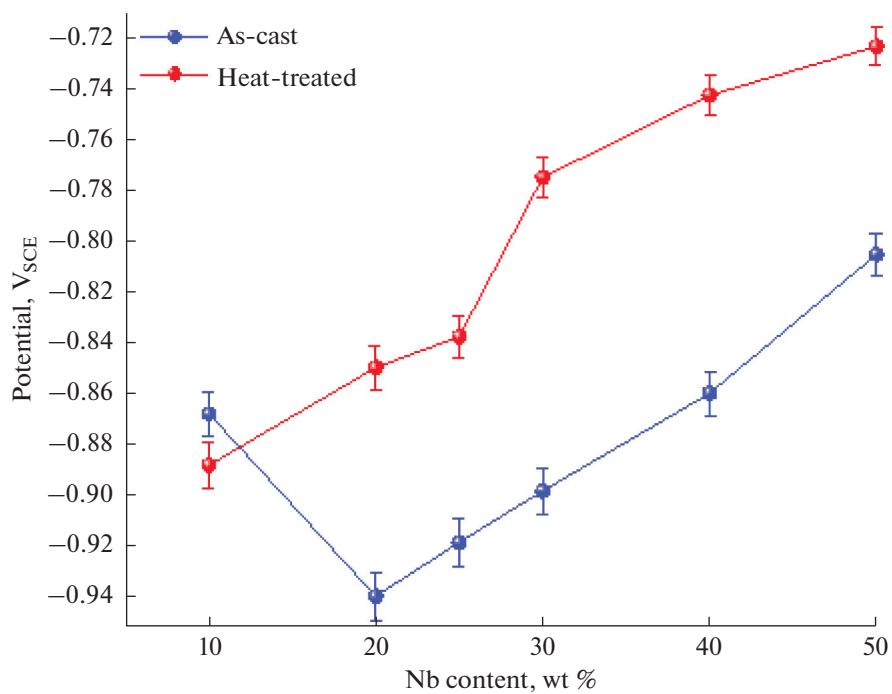
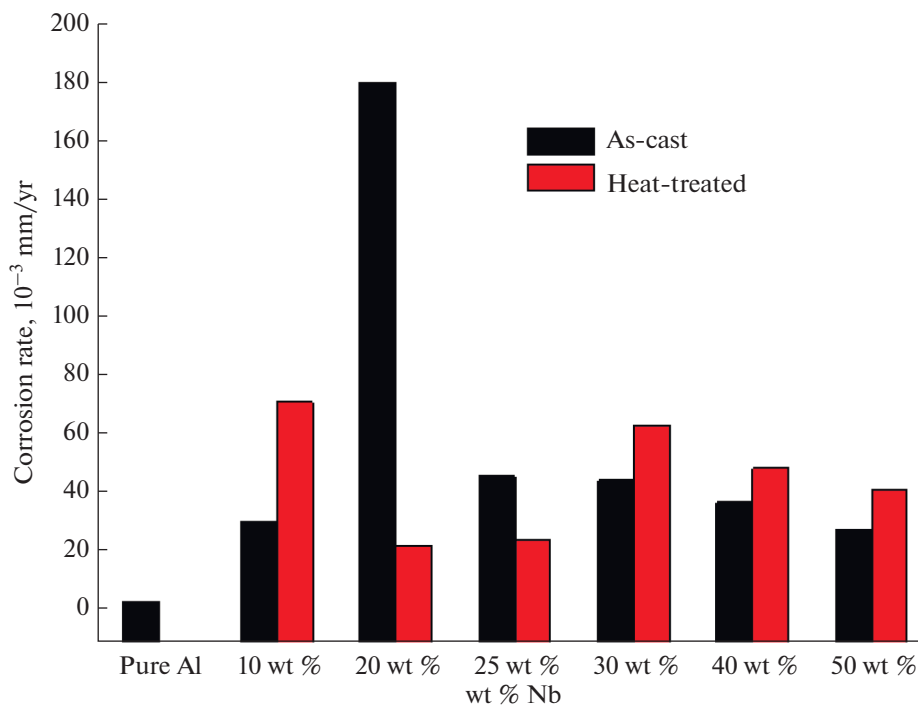**Fig. 9.** Potential variation versus Nb content (as-cast and heat-treated).

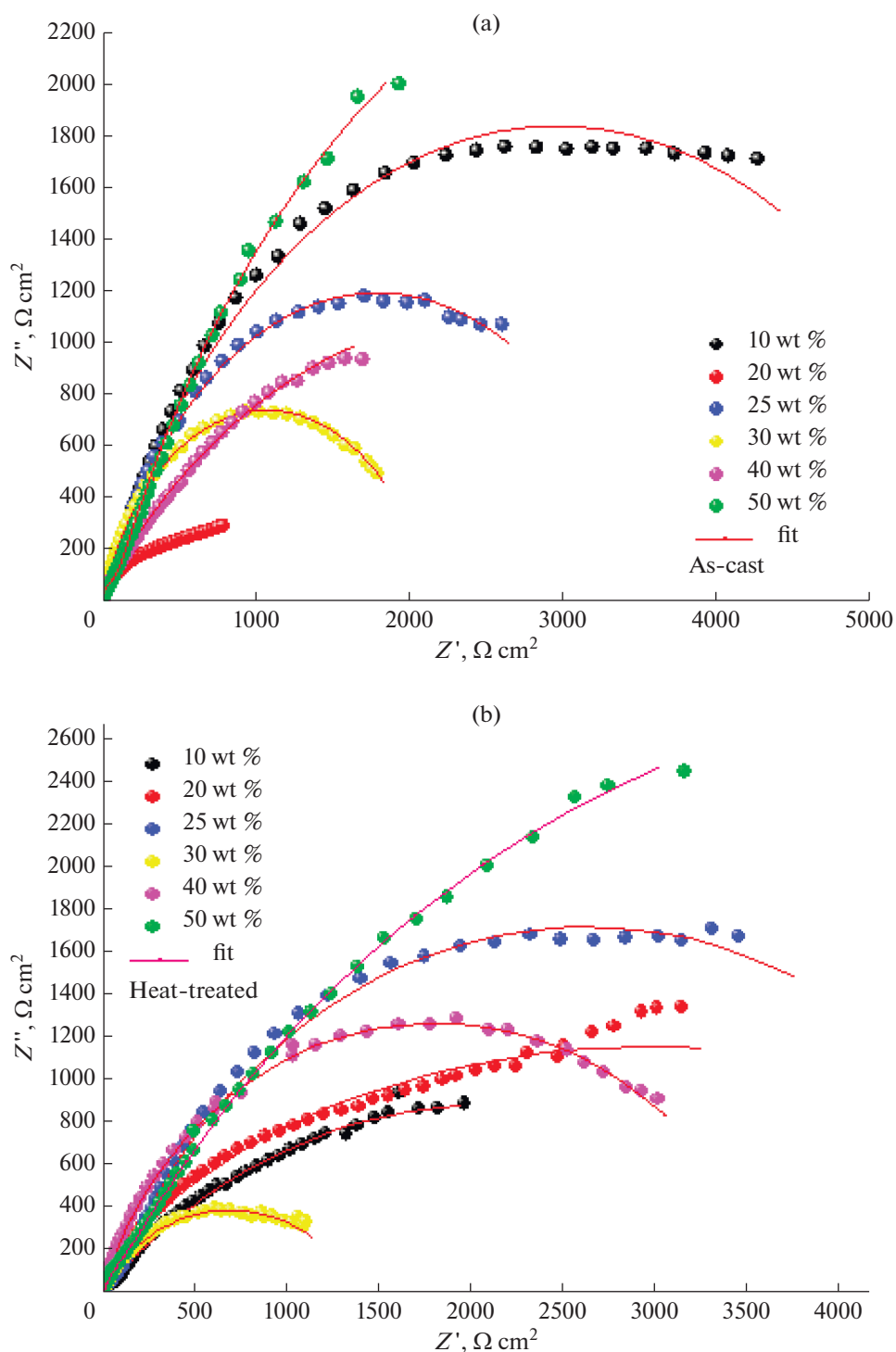**Fig. 10.** Corrosion rate variation versus Nb content (as-cast and heat-treated).

Fig. 11. Experimental EIS diagrams of Al–Nb as-cast (a) and heat-treated alloys; (b) in medium 3.5 wt % NaCl at room temperature Nyquist plot.

corrosion inhibitors at the site of damage [60] and can however lead to a self-healing behavior. Different behaviors can be at the origin of the type of corrosion depending on the niobium content of the alloy and

therefore the volume fraction and the morphology of the Al_3Nb phase or the microstructure [61, 62]. This can range from pitting corrosion as in the case of alloy 10 wt %, pitting initiates at defects on the surface of the
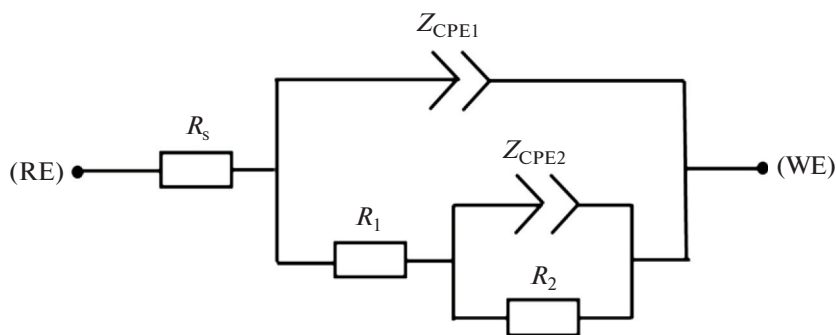
Fig. 12. Equivalent electrochemical circuit of Al−Nb alloys in medium 3.5 wt % NaCl at room temperature.

aluminium, such as at second phase particles, to crevice corrosion alloy 20 wt % or intergranular corrosion alloy 50 wt % which is caused by potential differences between the grain-boundary region formed exclusively by α-aluminium and the adjacent grain boundaries or Al$_3$Nb pavement Figs. 13k, 13l. On the other hand, the presence of the Al$_3$Nb intermetallic phase in large quantities can also be responsible for a galvanic cou-

Table 9. Electrochemical impedance parameters

| Alloy	R_1, Ω cm^2	F, μF cm^{-2}	n_1	R_s, Ω cm^2	F, μF cm^{-2}	n_2	R_2, Ω cm^2
(a) of Al−Nb as-cast with different Nb content 3.5% NaCl solution at room temperature							
10 wt % as-cast	7.982	23.51	0.74	14.71	104.5	0.69	5958
20 wt % as-cast	5.203	92.91	0.84	2.46	1146	0.24	6703
25 wt % as-cast	5.16	52	0.86	45.64	147.2	0.71	3564
30 wt % as-cast	4.531	18.42	0.99	8.57	184.5	0.73	2171
40 wt % as-cast	4.973	23.43	0.94	10.05	396.9	0.53	4279
50 wt % as-cast	3.208	36.34	0.99	123.1	404.2	0.72	8078
(b) of Al−Nb heat-treated with different Nb content 3.5% NaCl solution at room temperature							
10 wt % heat-treated	5.70	69.94	0.66	29.55	285.9	0.46	4275
20 wt % heat-treated	5.92	15.69	0.87	22	177.7	0.40	6452
25 wt % heat-treated	5.15	27.3	0.83	97.1	117.5	0.72	5135
30 wt % heat-treated	4.25	39.98	0.89	6.601	281.7	0.58	1423
40 wt % heat-treated	4.738	20.13	0.99	15.35	110	0.70	3670
50 wt % heat-treated	4.857	53.99	0.87	216.1	225	0.60	10324
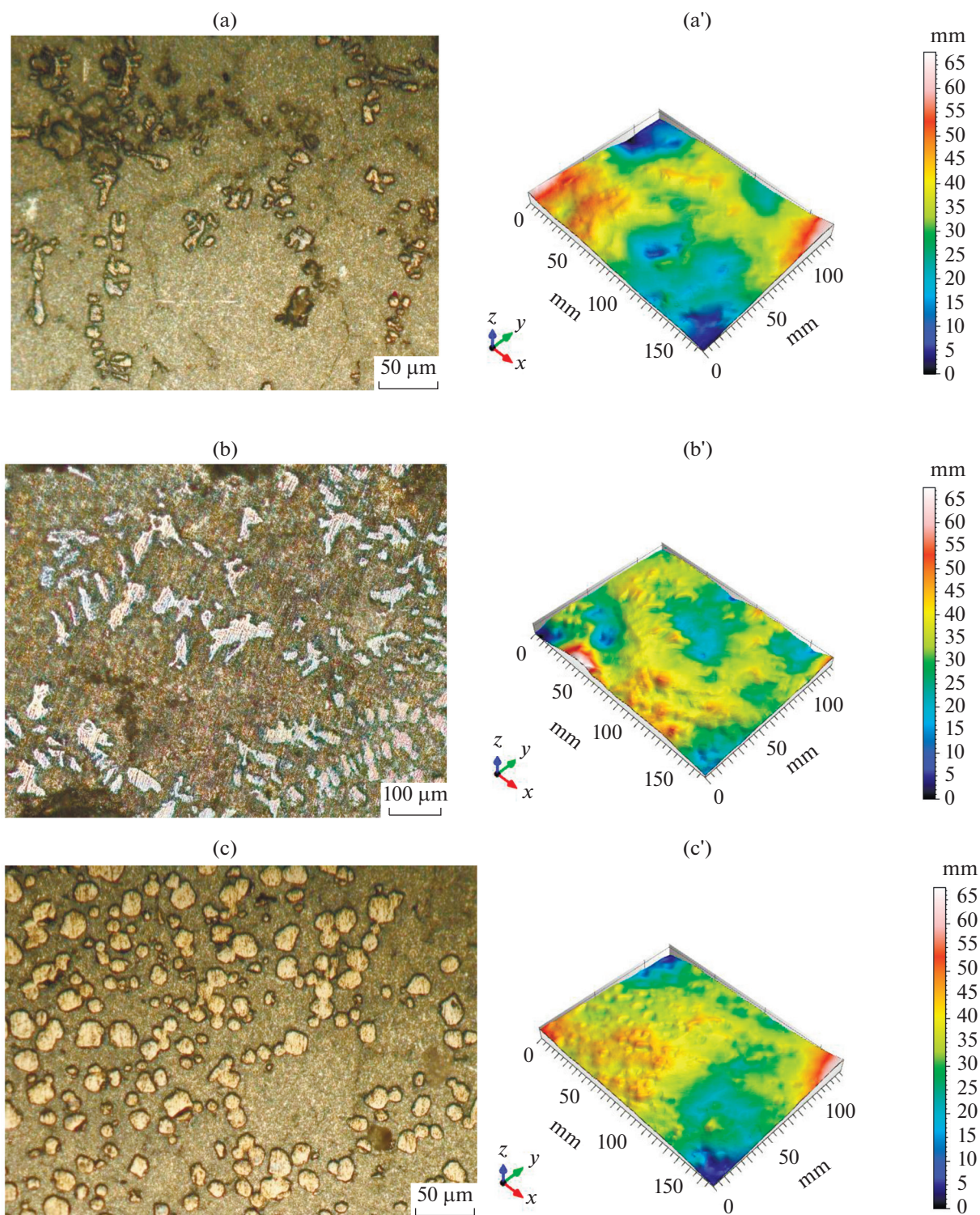
Fig. 13. Optical micrographs with associated 3D surface morphology (as-cast alloys): (a–a') 10 wt % before corrosion, (b–b') 10 wt % after corrosion, (c–c') 20 wt % before corrosion, (d–d') 20 wt % after corrosion, (e–e') 25 wt % before corrosion, (f–f') 25 wt % after corrosion (g–g') 30 wt % before corrosion, (h–h') 30 wt % after corrosion, (i–i') 40 wt % before corrosion, (j–j') 40 wt % after corrosion, (k–k') 50 wt % before corrosion, (l–l') 50 wt % after corrosion.
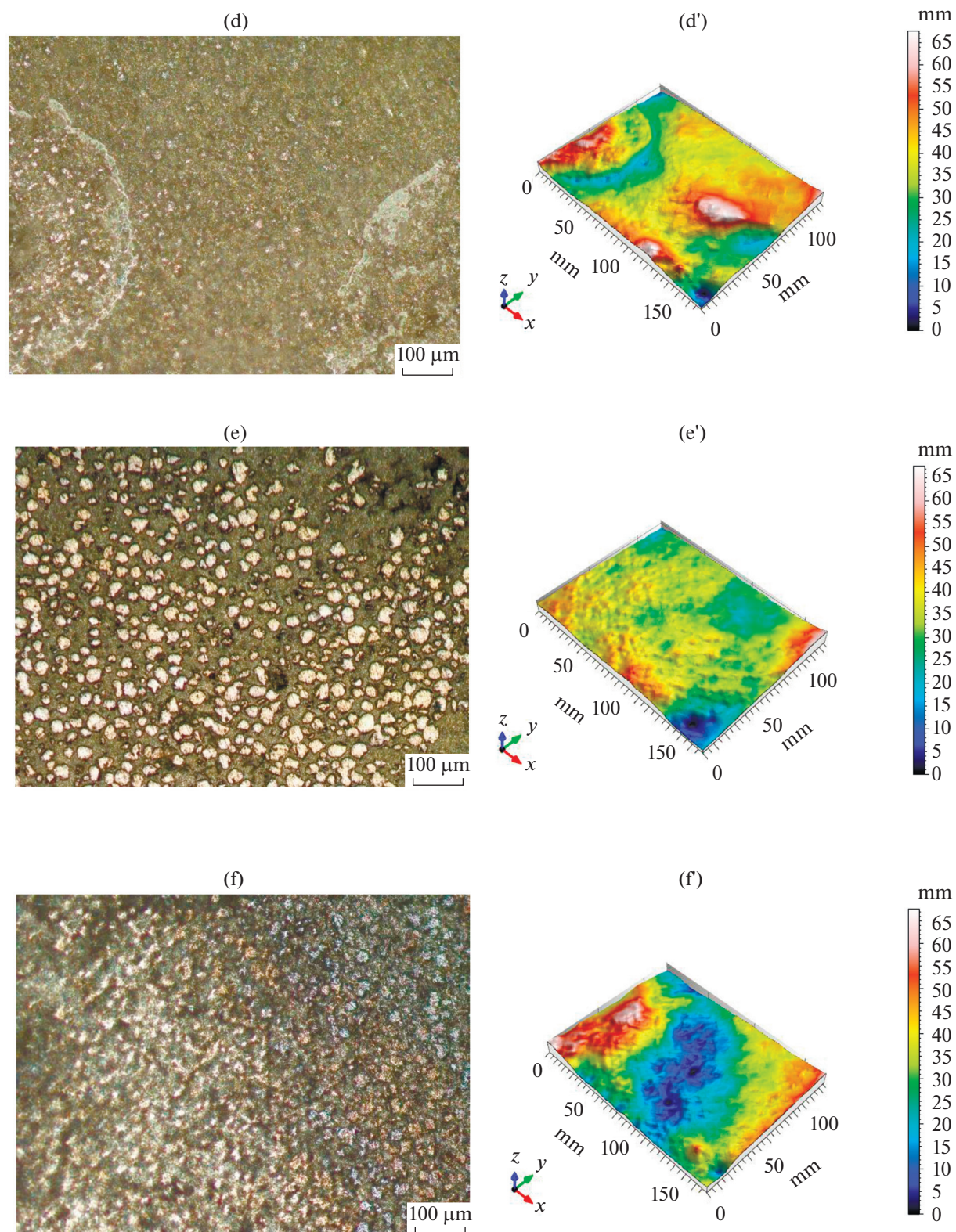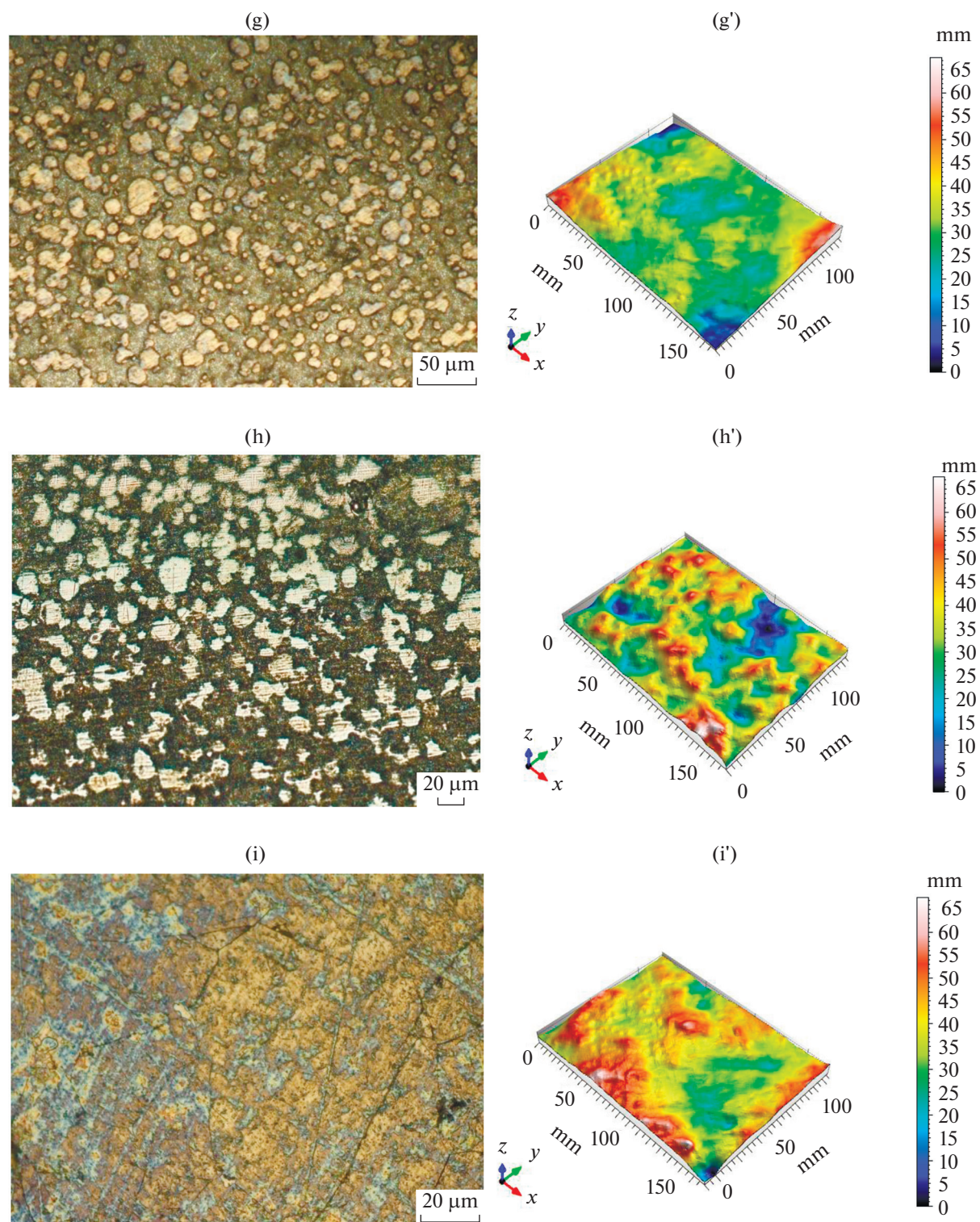
Fig. 13. (Contd.)

(g)

(g')
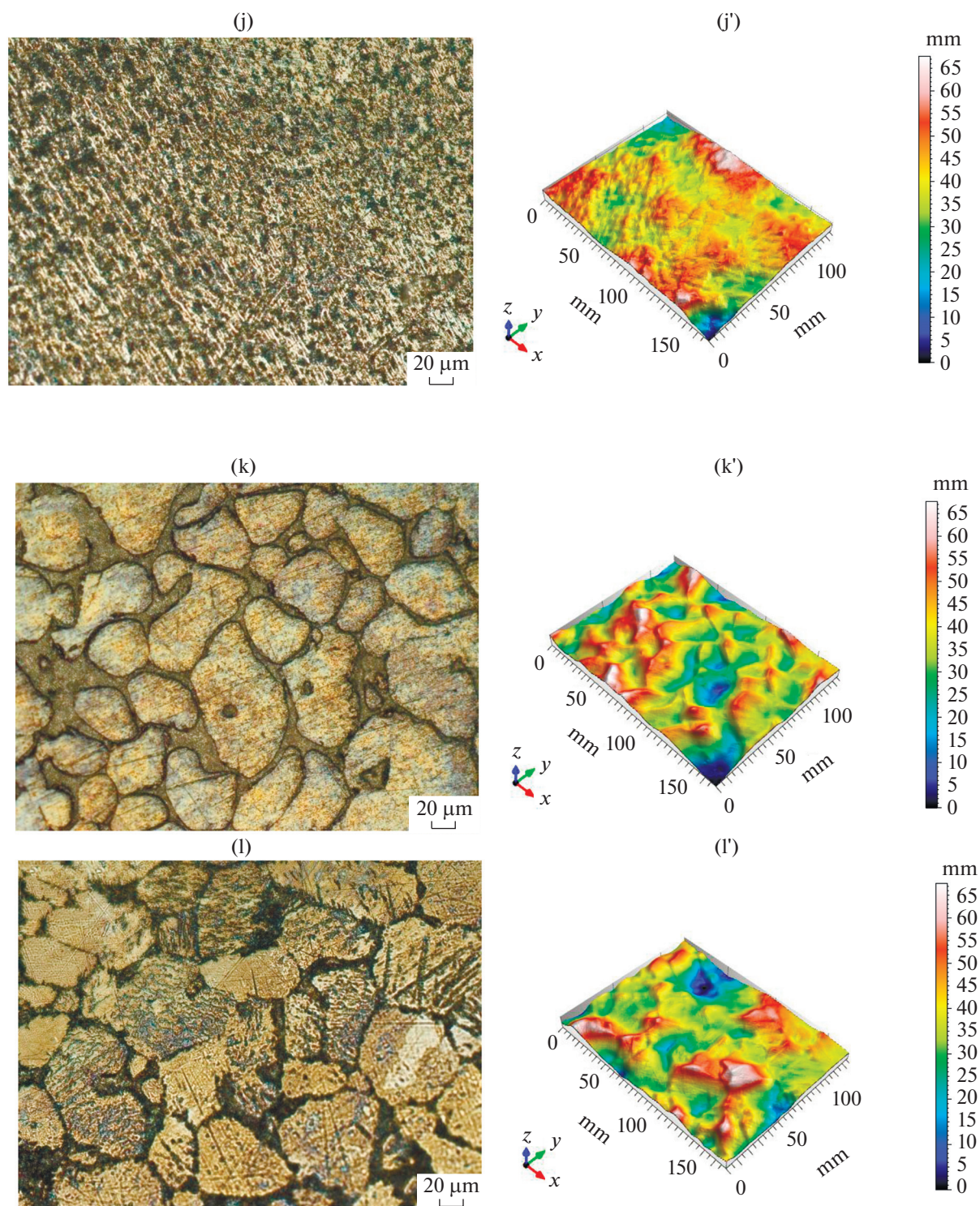
(h)

(h')

(i)

(i')

Fig. 13. (Contd.)

Fig. 13. (Contd.)

pling between the matrix and the second phase particles [62]. Active components of the matrix alloy and the intermetallic phases may corrode selectively.

CONCLUSIONS

This work covers results regarding the effect of niobium addition on aluminum synthesized by the high-frequency induction fusion technique. The main concluding remarks are as below:

(1) X-ray diffraction and thermal analysis show that as-cast and heat-treated Al−Nb alloys crystallize in a mixture of Al_3Nb and Al (Nb) solid solution.

(2) Al_3Nb intermetallic compound dispersed in the solid solution fcc α-Al matrix and associated with heat treatment plays a key role in corrosion resistance improvement of Al−Nb system by obstructing the potential sites for possible pitting corrosion which would be disastrous for the material. This preventive effect is all the more visible as the niobium content is high, as is the case of the alloy containing 50 wt % Al.

(3) Alloy 50 wt % is the niobium richest and its structure is totally different from that of other alloys both in the as-cast and in the heat-treated states. A α-Al solid solution is reduced to a minor phase and therefore confines in the Al_3Nb inter-particle spacing.

(4) Alloy 50 wt % as-cast and alloy 20 wt % heat treated 1 h at 500°C, show the best results concerning corrosion in a saline medium (3.5 g/L NaCl). The effect of heat-treatment is to change the distribution and volume fraction of the intermetallic phase, so that after heat treatment an alloy may end up with improved corrosion resistance compared to the raw state.

CONFLICT OF INTERESTS

Authors announce that there is no conflict of interest.

REFERENCES

1. Audebert, F., Galano, M., and Saporiti, F., The use of Nb in rapid solidified Al alloys and composites, *J. Alloys Compd.,* 2014, vol. 615, p. 621.

2. Schwarz, H.G., Briem, S., and Zapp, P., Future carbon dioxide emissions in the global material flow of primary aluminium, *Energy,* 2001, vol. 26, p. 775.

3. Hirsch, J., Aluminium in innovative light-weight car design, *Mater. Trans.,* 2011, vol. 52, p. 818.

4. Toros, S., Ozturk, F., and Kacar, I., Review of warm forming of aluminum−magnesium alloys, *J. Mater. Process. Technol.,* 2008, vol. 207, p. 1.

5. Yasakau, K.A., Zheludkevich, M.L., and Ferreira, M.G.S., Role of intermetallics in corrosion of aluminum alloys. Smart corrosion protection, in *Intermetallic Matrix Composites,* Mitra, R., Ed., Woodhead Publ., 2018, p. 425.

6. Ujah, C.O., Popoola, A.P.I., Popoola, O.M., and Aigbodion, V.S., Electrical conductivity, mechanical strength and corrosion characteristics of spark plasma sintered Al−Nb nanocomposite, *Int. J. Adv. Manufact. Technol.,* 2019, vol. 101, p. 2275.

7. Pramod, S.L., Bakshi, S.R., and Murty, B.S., Aluminum-based cast in situ composites: a review, *J. Mater. Eng. Perform.,* 2015, vol. 24, p. 2185.

8. Di Franco, F., Santamaria, M., Di Quarto, F., La Mantia, F., de Sá, A.I., and Rangel, C.M., Dielectric properties of Al−Nb amorphous mixed oxides, *ECS J. Solid State Sci. Technol.,* 2013, vol. 2, p. 205.

9. Saidman, S.B., Garcia, S.G., and Bessone, J.B., Electrochemical behaviour of Al−In alloys in chloride solutions, *J. Appl. Electrochem.,* 1995, vol. 25, p. 252.

10. Salinas, D.R., Influence of alloying elements and microstructure on aluminium sacrificial anode performance: case of Al±Zn, *J. Appl. Electrochem.,* 1999, vol. 29, p. 1063.

11. Shayeb, H.A.E., Effect of gallium ions on the electrochemical behaviour of Al, Al±Sn, Al±Zn and Al±Zn±Sn alloys in chloride solutions, *Corros. Sci.,* 2001, vol. 43, p. 643.

12. Gudić, S., Smoljko, I., and Kliškić, M., Electrochemical behaviour of aluminium alloys containing indium and tin in NaCl solution, *Mater. Chem. Phys.,* 2010, vol. 121, p. 561.

13. Shibli, S.M.A., Jabeera, B., and Manu, R., Development of high performance aluminium alloy sacrificial anodes reinforced with metal oxides, *Mater. Lett.,* 2007, vol. 61, p. 3000.

14. Mostaan, H., Karimzadeh F., and Abbasi, M.H., Thermodynamic analysis of nanocrystalline and amorphous phase formation in Nb−Al system during mechanical alloying, *Powder Metall.,* 2012, vol. 55, p. 142.

15. Gauthier, V., Bernard, F., Gaffet, E., Vrel, D., Gailhanou, M., and Larpin, J.P., Investigations of the formation mechanism of nanostructured $NbAl_3$ via MASHS reaction, *Intermetallics,* 2002, vol. 10, p. 377.

16. Almeida, A., Petrov, P., Nogueir I., and Vilar, R., Structure and properties of Al−Nb alloys produced by laser surface alloying, *Mater. Sci. Eng. A,* 2001, vol. 303, p. 273.

17. Vilar, R., Conde, O., and Franco, S., Crystallographic structure of Al_3Nb in laser-processed Al−Nb alloys, *Intermetallics,* 1999, vol. 7, p. 1227.

18. Baumann, J.R., Liebemann, E.K., Simon, M., and Bucher, E., Growth, structural study, and thermal stability of metallic Al/Nb superlattices, *Phys. Rev. B,* 1992, vol. 45, p. 3778.

19. Wang, N., Chao, D., Hou, J., Zhang, Y., Huang, K., Jiao, S., and Zhu, H., Direct synthesis of Nb−Al inter-

metallic nanoparticles by sodiothermic homogeneous reduction in molten salts, *Intermetallics,* 2013, vol. 43, p. 45.

20. Miao, W., Tao, K., Liu, B.X., and Li, B., Formation of NbAl₃ by Nb ion implantation using metal vapor vacuum arc ion source, *Nucl. Instrum. Methods Phys. Res. Sect. B: Beam Interact. Mater. Atoms,* 2000, vol. 160, p. 343.

21. Santamaria, M., Di Franco, F., Di Quarto, F., Skeldon, P., and Thompson, G.E., Tailoring of the solid state properties of Al−Nb mixed oxides: a photoelectrochemical study, *J. Phys. Chem. C,* 2013, vol. 117, p. 4201.

22. De Sá, A.I., Rangel, C.M., Smith, C.J.E., Skeldon, P., and Thompson, G.E., Growth of anodic oxides on sputtered Al−Nb alloys, *Key Eng. Mater.,* 2002, vol. 230, p. 44.

23. Wang, F., Liang, Y.F., Shang, S.L., Liu, Z.K., and Lin, J.P., Nb−Al diffusion reaction in high Nb containing TiAl porous alloys, *Mater. Sci. Technol.,* 2015, vol. 31, p. 1388.

24. Peng, L.M., Synthesis and mechanical properties of niobium aluminide-based composites, *Mater. Sci. Eng. A,* 2008, vol. 480, p. 232.

25. De Lazzari, C.P., Danielle Goya Simões, D., and Trani Capocchi, J.D., Study of the aluminothermic reduction of niobium pentoxide through thermal analysis experiments and high energy milling processing, *Mater. Res.,* 2007, vol. 10, p. 215.

26. Yeh, C.L. and Wang, H.J., Effects of sample stoichiometry of thermite-based SHS reactions on formation of Nb−Al intermetallics, *J. Alloys Compd.,* 2009, vol. 485, p. 280.

27. Sina, H. and Iyengar, S., Studies on the formation of aluminides in heated Nb−Al powder mixtures, *J. Alloys Compd.,* 2015, vol. 628, p. 19.

28. Fleischer, R.L., Field, R.D., Denike, K.K., and Zabala, R.J., Mechanical properties of alloys of IrNb and other high-temperature intermetallic compounds, *Metallurg. Trans. A,* 1990, vol. 21, p. 306.

29. Jiao, Z., Li, C., Bai, Y., Zhang, M., Liu, Q., Ling, X., Gong, Y., Liu, F., and Liu, Z., A comparative study of NbAl₃ and Nb₃Al itermetallic compounds under pressure, *Comput. Mater. Sci.,* 2017, vol. 126, p. 280.

30. Khireche, S., Boughrara, D., Kadri, A., Hamadou L., and Benbrahim, N., Corrosion mechanism of Al, Al−Zn and Al−Zn−Sn alloys in 3 wt % NaCl solution, *Corros. Sci.,* 2014, vol. 87, p. 504.

31. Gupta, R.K., Fabijanic, D., Zhang, R., and Birbilis, N., Corrosion behaviour and hardness of in situ consolidated nanostructured Al and Al−Cr alloys produced via high-energy ball milling, *Corros. Sci.,* 2015, vol. 98, p. 643.

32. Oladijo, O.P., Obadele, B.A., Venter, A.M., and Cornish, L.A., Investigating the effect of porosity on corrosion resistance and hardness of WC−Co coatings on metal substrates, *Afr. Corros. J.,* 2016, vol. 2, p. 37.

33. Decheng, K., Chaofang, D., Xiaoqing, N., Liang, Z., Cheng, M., Jizheng, Y., Yucheng, J., Yupeng, Y., Kui, X., Xuequn, C., and Xiaogang, Li, High-throughput fabrication of nickel-based alloys with different Nb contents via a dual-feed additive manufacturing system: effect of Nb content on microstructural and mechanical properties, *J. Alloys Compd.,* 2019, vol. 785, p. 826.

34. Okamoto, H., Supplemental literature review of binary phase diagrams: Ag−Nd, Ag−Zr, Al−Nb, B−Re, B−Si, In−Pt, Ir−Y, Na−Si, Na−Zn, Nb−P, Nd−Pt, and Th−Zr, *J. Phase Equilib. Diffus.,* 2014, vol. 35, p. 636.

35. Witusiewicz, V.T., Bondar, A.A., Hecht, U., Rex, S., and Velikanova, T.Y., The Al−B−Nb−Ti system: III. Thermodynamic re-evaluation of the constituent binary system Al−Ti, *J. Alloys Compd.,* 2008, vol. 465, p. 64.

36. He, C., Stein, F., and Palm, M., Thermodynamic description of the systems Co−Nb, Al−Nb and Co−Al−Nb, *J. Alloys Compd.,* 2015, vol. 637, p. 36.

37. Carvalho Coelho, G., Angelo Nunes, C., Fiorani, J.M., David, N., and Vilasi, M., *Mat. Res.,* 2019, vol. 22, p. 1.

38. Jorda, J.L., lükiger, R.F., and Muller, J., A New metallurgical investigation of the niobium−aluminium system, *J. Less Common. Met.,* 1980, vol. 75, p. 227.

39. Ribaud, G., La théorie du chauffage par courants induits de haute fréquence, *J. Phys. Radium,* 1932, vol. 3, p. 537.

40. Souilah, Y., Boutouta, A., Boulkhessaim, S., Bedboudi, H., Bourbia, A., and Draissia, M., Correlation of hardness and corrosion characteristics with crystalline structures of Al−Mg alloys, *Phys. Scr.,* 2013, vol. 88, p. 06560.

41. Knipling, K.E., Dunand, D.C., and Seidman, D.N., Criteria for developing castable, creep-resistant aluminum-based alloys—a review, *Z. Metallkd.,* 2006, vol. 97, no. 3, p. 246.

42. George, E., Totten, D., and MacKenzie, S., *Handbook of Aluminum,* vol. 2: *Alloy Production and Materials Manufacturing,* CRC Press, 2003, p. 736

43. Prach, O., Trudonoshyn, O., and Puchnin, M., Effects of chemical composition on mechanical properties of Al−Mg−Si−Mn based alloys materials engineering, *Mater. Inž.,* 2017, vol. 24, p. 11.

44. Car, T., Radić, N., Panjan, P., and Tonejc, A., Mehanical properties of Al−(Nb, Mo, Ta, W) thin films, *Strojarstvo,* 2011, vol. 53, p. 429.

45. Osório, W.R., Freire, C.M., and Garcia, A., The effect of the dendritic microstructure on the corrosion resistance of Zn−Al alloys, *J. Alloys Compd.,* 2005, vol. 397, p. 179.

46. Osório, W.R., Santos, C.A., Quaresma, J.M.V., and Garcia, A., Mechanical properties as a function of thermal parameters and microstructure of Zn−Al castings, *J. Mater. Process. Technol.,* 2003, vol. 143-144, p. 703.

47. Donelan, P., Modelling microstructural and mechanical properties of ferritic ductile cast iron, *Mater. Sci. Technol.,* 2000, vol. 16, p. 261.

48. Quaresma, J.M.V., Santos, C.A., and Garcia, A., Correlation between unsteady-state solidification conditions, dendrite spacings, and mechanical properties of Al−Cu alloys, *Metall. Mater. Trans. A,* 2000, vol. 31, p. 3167.

49. Khun, N.W. and Liu, E., Effect of substrate temperature on corrosion performance of nitrogen doped amorphous carbon thin films in NaCl solution, *Thin Solid Films,* 2009, vol. 517, p. 4762.

50. Benzarouk, H., Drici, A., Mekhnache, M., Amara, A., Guerioune, M., Bernède, J.C., and Bendjffal, H., Effect of different dopant elements (Al, Mg, and Ni) on microstructural, optical and electrochemical properties of ZnO thin films deposited by spray pyrolysis (SP), *Superlattices Microstruct.,* 2012, vol. 52, p. 594.

51. Enos, D.G., The potentiodynamic polarization scan, *Tech. Rep. no. 33,* Center for Electrochemical Science & Engineering. Department of Materials, 1997.

52. Wong, L.L., Martin, S.I., and Rebak, R.B., Methods to calculate corrosion rates for alloy from polarization resistance experiments, *Proc. ASME 2006 Pressure Vessels and Piping/ICPVT-11 Conf.,* Vancouver, 2006.

53. Shi, Y.Z., Yang, B., Xie, X., Brechtl, J., Dahmen, K.A., and Liaw, P.K., Corrosion of Al$_x$CoCrFeNi high-entropy alloys: Al content and potential scan-rate dependent pitting behavior, *Corros. Sci.,* 2017, vol. 33, p. 119.

54. Singh, D., Dhayal, V., and Chandra, D.A., Corrosion performance of nano-alumina coatings over anodized aluminum alloy by dip coating method, *Surf. Eng. Appl. Electrochem.,* 2019, vol. 55, p. 436.

55. Toloei, A. and Stoilov, V.D., *Northwood Proc. ASME 2013 Int. Mechanical Engineering Congress & Exposition IMECE2013,* San Diego, CA, Nov. 13–21, 2013.

56. Chen, Y. and Jepson, W.P., EIS measurement for corrosion monitoring under multiphase flow conditions, *Electrochim. Acta,* 1999, vol. 44, no. 24, p. 4453.

57. Prakashaiah, B.G., Vinaya Kumara, D., Anup Pandith, A., Nityananda Shetty, A., and Amitha Rani, B.E., Corrosion inhibition of 2024-T3 aluminum alloy in 3.5% NaCl by thiosemicarbazone derivatives, *Corros. Sci.,* 2018, vol. 136, p. 326.

58. Arthanari, S., Jang, J.C., and Shin, K.S., Corrosion performance of high pressure die-cast Al−Si−Mg−Zn alloys in 3.5 wt % NaCl solution, *J. Alloys Compd.,* 2019, vol. 783, p. 494.

59. Song, G.L. and Liu, M., Corrosion and electrochemical evaluation of an Al−Si−Cu aluminum alloy in ethanol solutions, *Corros. Sci.,* 2013, vol. 72, p. 73.

60. Wen, J., Cui, H., Wei Na, Song, X., Zhang, G., Wang, C., and Song, Q., Effect of phase composition and microstructure on the corrosion resistance of Ni−Al intermetallic compounds, *J. Alloys Compd.,* 2017, vol. 695, p. 2424.

61. Gupta, R.K., Murty, B.S., and Birbilis, N., Corrosion behaviour of high-energy ball milled, anocrystalline Al alloys, in *An Overview of High-Energy Ball Milled Nanocrystalline Aluminum Alloys,* Cham: Springer Int. Publ., 2017.

62. Kharitonov, D.S., Sommertunec, J., Örneka, C., Ryld, J., Kuriloe, I., Claessona, P.M., and Pana, J., Corrosion inhibition of aluminum alloy AA6063-T5 by vanadates: microstructure characterization and corrosion analysis, *J. Electrochem. Soc.,* 2018, vol. 165, p. 116.